Journal of *Marine Science and Engineering*

MDPI

Article

A Risk Assessment of Underwater Cultural Heritage for Wave-Induced Hazards: The Impact of Climate Change on Cadiz Bay

C. Ferrero-Martín [1,*], A. Izquierdo [1], M. Bethencourt [2] and T. Fernández-Montblanc [3,*]

[1] Department of Applied Physics, University of Cadiz, INMAR, 11510 Cadiz, Spain; alfredo.izquierdo@uca.es
[2] Department of Materials Science, Metallurgical Engineering and Inorganic Chemistry, University of Cadiz, INMAR, 11510 Cadiz, Spain; manuel.bethencourt@uca.es
[3] Earth Sciences Department, University of Cadiz, INMAR, 11510 Cadiz, Spain
* Correspondence: carmen.ferrero@uca.es (C.F.-M.); tomas.fernandez@uca.es (T.F.-M.)

Abstract: The combination of future changes in sea levels and wave climate in coastal areas represents one of the greatest threats to the preservation of underwater cultural heritage (UCH). This study presents a new methodology to assess climate change's impacts on UCH preservation in shallow waters, focusing on wave-induced hazards like decontextualization, scouring, and wear erosion. The approach uses hybrid downscaling of bias-corrected wave fields from the RCP4.5 and RCP8.5 CMIP5 scenarios. The methodology was applied in the Bay of Cadiz, where an overall reduction in wave energy flux was observed. However, local increases were detected in rocky outcrops and coastal areas with high UCH density. As a result, the shallow zones exhibited significant changes in decontextualization and scouring hazards. However, the most relevant risk changes were linked to wear erosion, particularly at sites on rocky outcrops near Cadiz. The methodology proposed in this study is essential for identifying areas with higher risk and for evaluating UCH preservation under future climate conditions. It offers an effective tool for discriminating sites at risk and for conducting a long-term assessment of these risks in coastal environments affected by climate change.

Keywords: underwater cultural heritage; climate change; hybrid downscaling; decontextualization risk; scouring risk; wear erosion risk, numerical modelling, ocean waves

check for updates

Academic Editor: Eugen Rusu

Received: 29 November 2024
Revised: 29 December 2024
Accepted: 30 December 2024
Published: 14 January 2025

Citation: Ferrero-Martín, C.; Izquierdo, A.; Bethencourt, M.; Fernández-Montblanc, T. A Risk Assessment of Underwater Cultural Heritage for Wave-Induced Hazards: The Impact of Climate Change on Cadiz Bay. *J. Mar. Sci. Eng.* **2025**, *13*, 136. https://doi.org/10.3390/jmse13010136

1. Introduction

The alterations in wave climate attributable to global warming are of vital importance in coastal areas given the fundamental role of waves in shaping coastal dynamics and coastal hazards. These modifications have the potential to change coastal morphology [1] and significantly impact human activities. Assessing the impacts resulting from climate change (CC) in littoral areas is of great interest as these regions not only represent the most densely populated areas but also holds high value in terms of underwater cultural heritage (UCH).

The preservation of UCH is crucial for local communities, and it is necessary to recognize and properly appreciate its value [2] as its degradation not only implies a loss of cultural capital but also reductions in tourism and recreational, educational, and scientific activities, as well as a decline in local ecological knowledge [3]. In this regard, within the framework of the European Green Deal, it is anticipated that the preservation of cultural heritage will serve as a powerful driver of economic recovery [4]. Littoral UCH is continuously subjected to the impact of marine agents that accelerate its degradation. Among these, waves stand out as one of the main factors affecting the preservation and

evolution of UCH in shallow water areas exposed to wave action [5,6]. Wave energy is released on the coast, generating three fundamental hazards for submerged cultural heritage: decontextualization, scouring, and wear erosion [7].

The complex interaction among archeological sites, suspended sediment transport, and hydrodynamic processes has been recognized and extensively investigated in the context of the in situ preservation of underwater archeological sites [5,6,8–13]. Changes in sediment budgets can compromise the stability of shipwrecks, leading to the exposure and/or burial of valuable artifacts. Additionally, scouring influences chemical and biological processes affecting the composition of the benthic community. This has effects on metallic materials [14], the corrosion rates of metal [15], and the degradation of stone materials [16] and wood [17].

CC will affect atmospheric and marine conditions, thereby impacting the conservation of coastal and underwater archeological sites. However, despite the relevance and high density of UCH in coastal areas, studies analyzing wave-induced hazards [7,18] have not considered long-term changes in environmental conditions.

Long-term changes in large-scale atmospheric circulation and in local wind patterns, coupled with changes in the occurrence and characteristics of tropical and extra-tropical cyclones, indicate long-term changes in wind wave statistics [19]. Reguero et al. [20] indicated that upper-ocean warming is altering the global wave climate, suggesting that global wave energy has increased by 0.4% per year since 1948. Global-scale studies have assessed projected changes in wave climate under different CC scenarios [21–23], finding a robust increase in the annual mean significant wave height in the Southern Hemisphere, while a reduction has been observed in the Northern Hemisphere. In the case of the North Atlantic, a reduction in significant wave height is expected by the end of the century, with greater decreases under the RCP8.5 scenario (~10%) compared to RCP4.5 (~5%) [24]. Furthermore, the extreme wave height is also projected to decrease in the northeast Atlantic [25–27], with the largest decrease being more than 1 m (12%) occurring south of 45° N [28].

These potential changes in global wave climate, along with sea level rise, underscore the need for further studies to downscale global trends regionally, analyze changes in wave climate in coastal shallow waters, and to evaluate how these changes will affect UCH preservation. Therefore, this study aims to develop a methodology to assess UCH-related risk associated with wave-induced hazards in current and future climates under climate change conditions. This methodology is tested in the Bay of Cadiz, a region characterized by a large number of UCH sites with great diversity. To achieve this, an assessment of wave climate and changes in the main hazards affecting UCH is carried out for the RCP 4.5 and RCP 8.5 scenarios. To attain the spatial resolution demanded by coastal applications and to reduce the uncertainties inherent in using global models for local-scale studies, a hybrid downscaling approach is employed to propagate waves from deep to shallow waters.

The remainder of this paper is structured as follows: The next section introduces the study area; the Methods Section describes the methodology developed and the datasets used for validation; the Results Section presents the downscaled wave climate and the assessment of CC's impact on UCH risks and hazards; the Discussion Section analyzes the applicability, limitations, and potential of the methodology based on the results; and, finally, the main findings of this study are summarized.

Study Area

The Bay of Cadiz is located in the southwest of Spain, extending from Punta Candor to the Sancti Petri estuary (Figure 1A). The seabed mainly consists of unconsolidated sediments, with a mean grain size ranging from very fine quartz sand to very fine gravel. Exceptions to this general pattern are localized rocky outcrops in the study area. The

bay is a mesotidal shallow estuary with a maximum depth of 20 m at its seaward edge, and it is characterized by dominantly semidiurnal co-oscillating tides with amplitudes of ~1 m for the M2 component and ~0.4 m for the S2 component [29]. The typical waves in the Bay of Cadiz are wind waves with periods below 7 s and significant heights around 0.5 m in summer and 1.0 m in winter, increasing during storm events. The longer swell components of the wave spectrum have periods of 12–15 s and a height of about 1.5 m [30]. The predominant wave direction is from the west, while the most energetic waves (wave heights exceeding the 95th percentile) originate from the west-southwest (Figure 1B). Winds in the Bay of Cadiz show significant seasonality with dominant Atlantic winds from the W and WNW, and less frequent but more intense Mediterranean winds from the ESE. S-SSW winds reaching speeds of 10–20 m·s^{-1} are associated with typical storm event conditions, occurring when low-pressure systems move along a SW-NE trajectory [6].

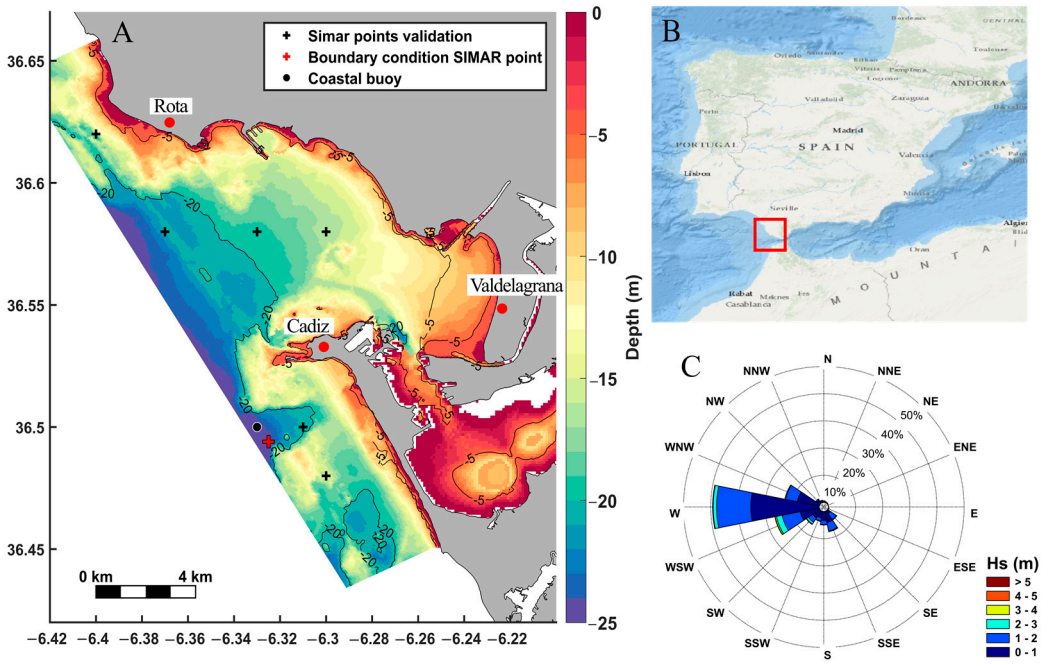

Figure 1. (**A**) Study area with overlaid bathymetry. (**B**) Location of the study area, Bay of Cadiz, Andalusia, Spain (**C**) A wave rose diagram of the significant wave height for a directional wave buoy.

The coastline stretching from the mouth of the Guadalquivir River to the Bay of Cadiz is one of the areas with the highest density of shipwrecks in the world owing to the presence of maritime trade routes since ancient times and the navigational hazards characteristic of this zone. The great archeological significance of Cadiz Bay drove their inclusion under the figure of maximum archeological protection of Andalusia in 2008 (BOJA nº48 of 03/10/2008, Resolution of 17 January 2008).

2. Methods

The proposed methodology for assessing the impact of climate change on the risk of UCH due to wave-induced hazards is structured into four phases (Figure 2). To better assess the temporal evolution of the risk, three time slices are considered: the baseline (1981–2005), the mid-century period (2036–2060), and the end-of-century (2075–2099) period. For each of these time slices, we create two climate change scenarios corresponding to the Representative Concentration Pathways (RCPs) defined in the Fifth Assessment Report (AR5) of the Intergovernmental Panel on Climate Change (IPCC): RCP4.5 and RCP8.5. RCP4.5 represents a moderate emission mitigation scenario, while RCP8.5 reflects a high-end, business-as-usual scenario.

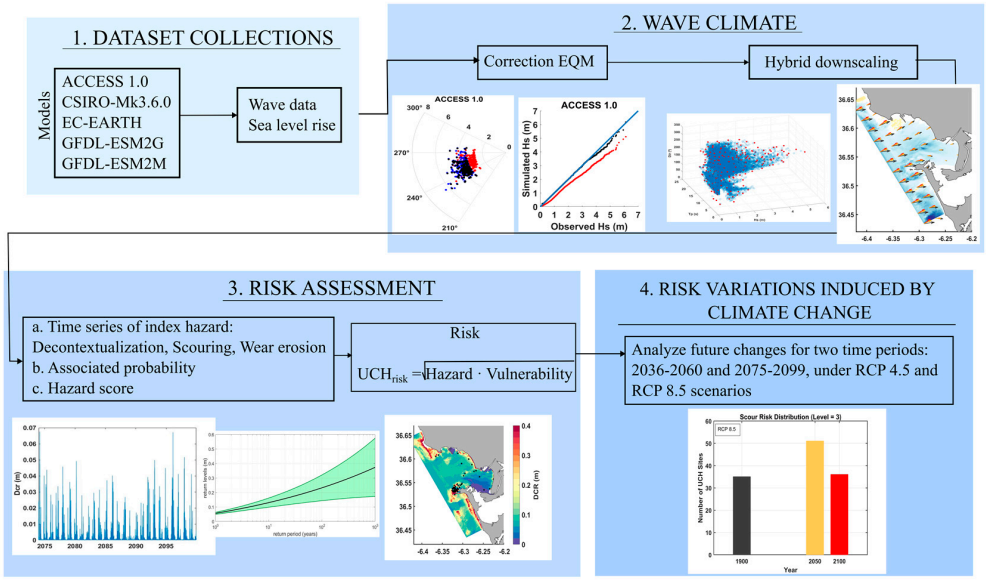

Figure 2. The workflow of the methodology developed to assess the impact of climate change on UCH risk due to wave-induced hazards.

In the first phase, time series of wave parameters and mean global sea level rise are extracted from the output of different global climate models corresponding to the historical runs and RCP4.5 and RCP8.5 climate change scenarios [31]. The second phase involves the treatment of RCP4.5 and RCP8.5 wave projections. This includes applying bias correction procedure, followed by propagating the bias-corrected wave field into shallow coastal waters using the hybrid downscaling method while considering sea level perturbation (tide + SLR). In the third phase, a risk assessment is performed for each of the considered hazards: decontextualization, scouring, and wear erosion. Finally, an ensemble mean is calculated using the variables and indices obtained for each of the global climate models, and the impacts of climate change on the risk are analyzed.

2.1. Datasets Collection

Wave Data and Sea Level Rise Projections

The historical wave data used in this study are detailed in Table 1. Given the temporal limitation of available data at the coastal buoy of Cadiz (6.33° W, 36.50° N, 21 m water depth), the buoy data are used to correct the longer timeseries from Med-Wav reanalysis [32] (maintained and distributed by the Copernicus Marine Service). The corrected Med-Wav reanalysis is then utilized for bias adjustment of the global climate model wave projection data (Table 2).

Table 1. Summary of wave data.

Name of Product	Spatial Resolution	Temporal Resolution	Available Period	Obser-Model	Bias Adjust	Institution
Coastal buoy of Cadiz	-	3 h (1996–1997)/ 1 h (1998–2014)	Scalar data: 1996–2019; directional data: 2001–2014	Obser.	none	Puertos del Estado
SIMAR	2.8 km	1 h	From 13-12-2005 to the present	Model	none	Puertos del Estado
MEDSEA-Wav	~4.6 km (1/24°)	1 h	1993–2016	Model	EQM by buoy	Copernicus Marine

Table 2. Wave and sea level rise projections. The table includes spatial and temporal atmospheric resolution, bias adjust applied, and affiliated institution.

Model	Atm. Spatial Resolution	Atm. Temporal Resolution	Bias Adjust	Institution
ACCESS 1.0	1.25° × 1.9°, L38	3 h	EQM by MEDSEA-WAVE	CSIRO and Bureau of Meteorology
CSIRO-Mk3.6.0	1.9° × 1.9°, L18	6 h	EQM by MEDSEA-WAVE	CSIRO, Industrial Research Organization & QCCCE
EC-EARTH	1.1° × 1.1°, L62	3 h	EQM by MEDSEA-WAVE	EC-EARTH consortium
GFDL-ESM2G	2° × 2.5°, L48	3 h	EQM by MEDSEA-WAVE	NOAA Geophysical Fluid Dynamics Laboratory
GFDL-ESM2M	2° × 2.5°, L48	3 h	EQM by MEDSEA-WAVE	NOAA Geophysical Fluid Dynamics Laboratory

The SIMAR reanalysis dataset (provided by Puertos del Estado) is used to validate the wave propagation methodology to shallow waters (downscaling) in the study area. The SIMAR dataset was generated by concatenating two simulated datasets, SIMAR-44 and WANA. To model wave fields over time, two third-generation models, WAM and WaveWatch III, are used with a nested grid scheme. These models are fed with wind data obtained from the HARMONIE-AROME mesoscale model provided by the State Meteorological Agency (AEMET, Spain). First, SIMAR point data (315047108) are used to propagate the wave time series into the Bay of Cadiz. The propagated wave field is then validated using data from SIMAR points located in intermediate waters at eight different locations within the study area (see Figure 1A). The validation period from 13 December 2005 to 1 May 2003 was selected based on the availability of SIMAR data.

The global wave projection data used in this study (Table 2) were generated using the spectral wave model WaveWatch III (version 4.18, [33]) forced by 10 m wind extracted from the Coupled Model Intercomparison Project Phase 5 (CMIP5) models ACCESS 1.0 (CSIRO-BOM, Australia), CSIRO-Mk3.6.0 (CSIRO-QCCCE, Australia), EC-EARTH (EC-EARTH consortium), GFDL-ESM2G, and GFDL-ESM2M (NOAA Geophysical Fluid Dynamics Laboratory USA). These models attain a horizontal resolution of 0.5° and a temporal resolution of 6 h [23]. The selection of these models is based on their high performance in reproducing synoptic situations and inter-annual variability across Europe [34]. CMIP5 models have a typical resolution of around 1°, which means they do not resolve tropical cyclones and poorly represent midlatitude storms [35].

In our analysis, sea level perturbation considers both tides and mean sea level. In CMIP models, ocean dynamic sea level (DSL) is diagnosed as ZOS [36]. However, DSL simulations from global climate models (GCMs) do not include the effect of sea level pressure on sea level (inverted barometer effect). ZOS varies locally due to ocean circulation and horizontal gradients, with its global mean being zero at every time step. As a result, ZOS excludes global mean sea level rise (GMSLR). The mean sea level, due to thermal expansion, changes in salinity affecting density, and water flows from the atmosphere, land, and glaciers, while always maintaining a constant total volume, is represented by ZOSGA. For this reason, as an approximation to sea level, we use the "adjusted ZOS," which is the sum of ZOS and ZOSGA. These variables were retrieved from the Earth System Grid (ESG) for the five global models previously mentioned. For the CSIRO-Mk360 model, ZOSTOGA (global mean thermosteric sea level rise; GMTSLR) is used instead of ZOSGA. Meanwhile, for the EC-EARTH model, only ZOS data are available. These are monthly data, so we interpolate them every 6 h and incorporate the tidal effect in order to later integrate them into the reconstruction of wave patterns within the bay. Furthermore, by using 3 h and 6 h wind fields to force wave models, much of the high-frequency nature of the wind climate is not

captured, which could lead to substantial errors when estimating the wave energy resource in a region [37].

2.2. Wave Climate Reconstruction

Global wave models are the most comprehensive tools available for simulating past and future wave climate on a global scale. However, they are unable to accurately simulate wave transformation processes in intermediate and shallow waters due to their limited spatial resolution. This limitation prevents the proper representation of bathymetric and coastal features, leading to systematic biases in the coastal zone.

2.2.1. Bias Adjustment of Global Wave Model

To mitigate these uncertainties, outputs from global wave models are corrected in two stages using wave buoy measurement and high-resolution wave reanalysis data (Med-WAV), involving both scalar and directional corrections. Since directional data from the buoy are limited and only available from 2001 onwards, we are unable to use directly observational data to correct the data from the global wave model, so the correction process is performed in two phases. First, the observational data (1983–2014) are used for the correction of the Med-WAV reanalysis at the location closest to the coastal buoy of Cadiz. Subsequently, in a second phase, the corrected Med-WAV model output (1993–2005) is used to adjust the bias in the global wave projections. The correction in both phases involves a scalar correction using the Empirical Quantile Mapping (EQM) method to address biases across different quantiles [38]. Subsequently, directional adjustment is carried out by dividing wave directions into 22.5° sectors. Within each sector, the difference between the mean directions of Med-WAV and global wave projections is calculated and applied as a correction [39]. The bias adjustment process is applied to the entire analysis period (baseline: 1981–2005; projections: 2006–2099), assuming that model biases and correction functions remain stationary over time.

2.2.2. Hybrid Downscaling

The adjusted global wave model time series are downscaled from deep water to shallow water using the hybrid downscaling methodology proposed by Camus et al. [40]. This approach combines a numerical wave model with statistical techniques and involves selecting a limited number of cases, within the range of 189 to 254 cases, based on the slide period and model. These cases ensure a proper representation of the possible sea states through bulk wave parameters (Hs, Tp, and Dir) and sea level (SL) in deep waters using a maximum dissimilarity selection algorithm. SL accounts for the tide and sea level rise associated with each period and model.

The selected sea states are propagated in the Bay of Cadiz using the third-generation wave model SWAN ("Simulating Waves Nearshore"; [41]). The spatial domain is discretized in a regular mesh with 37.5 m resolution. The mesh resolution is selected to balance the computational cost and the accurate representation of the bathymetric features (i.e., rocky outcrops, rocky shoals, and navigation channels) in the study area. We employ 36 directional bins ($\Delta\theta = 10°$) and 24 frequencies, with logarithmic spacing from 0.05 to 1.00 Hz. The range of the frequency is representative of the wave condition measured in the study area provided by the wave buoy used for the correction of MEDSEA-WAV reanalysis (2001–2014), where most of the data exhibit peak periods shorter than 20 s (see Figure 1 and [7]). The Battjes and Janssen [42] formula represents the depth-limited wave breaking. Then, the time series of the parameters of the propagated sea states are reconstructed at each node of the grid using an interpolation technique based on radial basis functions [40].

The effectiveness and accuracy of the EQM correction procedure and the wave propagation method are evaluated according to the following statistical indicators for scalar quantities:

- The correlation coefficient ro $= \sum_{i=1}^{N} (S_i - \overline{S})(R_i - \overline{R}) / \sigma_S \sigma_R$, where N denotes the number of data, S_i and R_i are simulations and reference data, σ_S and σ_R are their corresponding standard deviations, and the over bar denotes time averaging.
- The symmetrically normalized root mean square error, HH, introduced by Hanna and Heinold [43], $HH = \sqrt{\sum_{i=1}^{N} (S_i - R_i)^2 / \sum(S_i R_i)}$. This indicator combines information on the components of average error and dispersion and is characterized by not being biased towards simulations that underestimate the average [44].
- The root mean square error (RMSE), $RMSE = \sqrt{\frac{1}{N}\left[\sum_{i=1}^{N}(S_i - R_i)\right)]^2}$.
- The normalized root mean square error (NRMSE):

$$NRMSE = \sqrt{\frac{\sum_{i=1}^{N} (S_i - R_i)^2}{\sum_{i=1}^{N} (R_i)^2}}$$

- The bias (BIAS), $BIAS = \overline{S} - \overline{R}$.
- The normalized bias (NBI), $NBI = \sum_{i=1}^{N} (S_i - R_i) / \sum_{i=1}^{N} (R_i)$.
- The scatter index (SI), $SI = \sqrt{\frac{1}{N}\left[\sum_{i=1}^{N} (S_i - \overline{S})\right)(R_i - \overline{R})]^2} / \overline{R_i^2}$.

For the circular direction (θ), the normalized bias (NBI_θ) and the normalized root mean square error ($NRMSE_\theta$) are normalized by employing a 2π radians angle [45]:

- $NRMSE_\theta = \sqrt{\frac{\sum_{i=1}^{N} mod_{-\pi,\pi}\left(\theta_{Si} - \theta_{Ri})\right]^2 / N}{2\pi}}$
- $NBIAS_\theta = \sum_{i=1}^{N} mod_{-\pi,\pi}(\theta_{Si} - \theta_{Ri}\Big) / 2\pi N$ where the modulo operator $mod_{-\pi,\pi}$ indicates that if $(\theta_{Si} - \theta_{Oi}) > \pi$, a 2π angle is subtracted from the difference, and if $(\theta_{Si} - \theta_{Oi}) < -\pi$, a 2 π angle is added to the difference.

The skill scores are computed for the whole time series but also for the upper tail (>99th) in order to specifically evaluate the capability of the global wave model and downscaling methods to reproduce extreme wave conditions because of their large potential to damage UCH.

2.2.3. Bathymetry and Sediment Characterization

The bathymetry and seabed slope required for wave modeling were derived from multibeam echosounder data obtained during a comprehensive eco-cartographic study conducted in 2011 [46]. Additionally, seafloor mapping using multibeam backscatter data allowed for the classification of seafloor types, distinguishing between rocky and unconsolidated sediments. Sediment grain size was determined using 460 samples collected using a Van Veen grab.

2.2.4. Archeological Datasets

The archeological database, compiled by Fernández-Montblanc et al. [7], provides information about the main characteristics of UCH sites. This dataset includes attributes such as provenance and chronology; material composition (organized into five categories: metallic, stone, glass, ceramic, and wood/organic materials) and dominant material; metadata, including data source; and basic environmental characteristics of the sites, such depth and seabed type (when available). The archeological database comprises 56 sites of different chronologies spanning from 500 BC to AD 1820.

2.3. Risk Assessment

The risk assessment methodology evaluates UCH vulnerability to wave-induced hazards by calculating a risk index specific to each archeological site [7]. Each UCH site is treated as an asset susceptible to wave-induced damage.

The risk index is calculated as a function of vulnerability (determined by archeological materials, seabed slope, and type) and hazard. The analysis focuses on three primary wave-induced hazards that influence the long-term preservation of UCH: archeological decontextualization (DCR), scouring (SC), and erosive wear (EW). Each of these hazards is assessed independently without considering interactions between them. A response-based approach [47] is used, where hazard probability is directly calculated without presupposing underlying drivers or governing variables.

An indicator is defined for each hazard, and its assessment follows three sequential steps [48,49]. First, the time series of the hazard indicator are calculated based on the depth, seabed, grain size, wave characteristics, and sea level perturbation (tide + sea level rise). Second, extreme hazard probabilities are modeled using a transformed-stationary methodology. In this case, storm events are decluttered using a 72 h time window, and a constant threshold (97th percentile) is applied to select extreme events. The selected extreme events are fitted to a generalized Pareto distribution (see [50] for further details). For the case of archeological decontextualization and scour hazard, values corresponding to a 10-year return period are used as intermediate values in the extreme distribution. However, for the case of erosive wear hazard, a 1-year return period is selected to account for the continuous impact of wear on UCH materials. This reflects the high-frequency, cumulative damage of wear rather than isolated extreme events. Hazard indicators for each return period are ranked, and hazard scores (0 to 5) are assigned (see Table 3).

Table 3. Hazard indicator scores for decontextualization, scouring, and wear erosion.

Critical Size of Decontextualized Object, DCR (m) RT10	Scouring Volume, SV (m^3) RT10	Erosive Wear Potential, EWP (J/m^3) RT1	Scores	Level of Hazard
Dcr < 0.02	SV < 0.05	$-20 \geq$ EWP < -18	0	None
$0.02 \geq$ Dcr < 0.04	$0.05 \geq$ SV < 0.1	$-18 \geq$ EWP <-16	1	Low
$0.04 \geq$ Dcr < 0.08	$0.1 \geq$ SV < 0.15	$-16 \geq$ EWP < -13.5	2	Low/medium
$0.08 \geq$ Dcr < 0.12	$0.15 \geq$ SV <0.3	$-13.5 \geq$ EWP < -12.5	3	High/medium
$0.12 \geq$ Dcr < 0.16	$0.3 \geq$ SV < 0.4	$-12.5 \geq$ EWP < -11.5	4	High
Dcr $\geq$ 0.16	SV $\geq$ 0.4	EWP ≥ -11.5	5	Very high

RT10 corresponds to the value of a 10-year return period and RT1 to a 1-year return period.

Given the limited amount of information about UCH sites, we assume that all of them have the same exposure value. The risk index is calculated as the geometric square root of the product of the hazard and the vulnerability scores [48,51]. The vulnerability index ranges from 1 to 5 and is determined by the material composition of the UCH site and the specific hazard considered (refer to Table 4).

$$\text{UCHrisk} = \sqrt{\text{Hazard} \cdot \text{Vulnerability}} \quad (1)$$

Table 4. Vulnerability scores in common material in underwater cultural heritage sites for decontextualization, scouring, and wear erosion hazard.

	Material Category	Material Type	Vulnerability Score
Decontextualization	Metallic	Gray iron	1
	Stone	Marble	2
	Glass	Glass	3

Table 4. *Cont.*

	Material Category	Material Type	Vulnerability Score
Scouring	Ceramics	Coarse ware	4
	Wood/organic material	Oak	5
	Glass	Glass	1
	Metallic	Gray iron	2
	Ceramics	Coarse ware	3
	Stone	Marble	4
	Wood/organic material	Oak	5
Wear erosion	Stone	Marble	1
	Metallic	Gray iron	2
	Ceramics	Coarse ware	3
	Glass	Glass	4
	Wood/organic material	Oak	5

Sites are classified as "at risk" when $UCH_{Risk} > 3.2$, a threshold derived as the rounded geometric mean of "low" (2) and "very high" (5) classes. Higher UCH_{Risk} values indicate a combination of medium to very high vulnerability and hazard classes.

2.4. Wave Energy Flux

Wave energy flux (WEF) serves as comprehensive indicator of wave climate within the study area.

To account for water depth effects, the WEF calculation follows the methodology outlined by Liang et al. [52]:

$$WEF = \frac{\pi \rho g h H_s^2}{16 T_e}\left[1 + \frac{2kh}{\sinh(2kh)}\right] \quad (2)$$

where ρ is the water density, g is the gravitational acceleration, h is the water depth taking into account the sea level perturbation (tide and sea level rise), and H_s and T_e are the significant wave height and energy period, respectively, where T_e can be approximated as $T_e = T_p$. T_p denotes the peak period, while $k = 2\pi/L$ represents the wave number, and L is the wavelength. An extreme value analysis of the WEF time series is conducted for each grid node using the methodology in Section 2.3, focusing on a 10-year return period.

2.5. Variations in WEF and UCH Risk Induced by Climate Change

From the 5-member model ensemble, and for each considered period and scenario, we calculate the ensemble mean and standard deviation of WEF, hazard indices, and risk.

Model agreement is evaluated based on the coefficient of variation (CV) [53–55]. The CV is defined as the ratio of the standard deviation of the model ensemble, σ, to the ensemble mean value:

$$CV = \frac{\sigma_\alpha}{\overline{\alpha}} \quad (3)$$

where σ_α is the standard deviation of the model ensemble and $\overline{\alpha}$ is the ensemble mean. CV decreases as intra-model variability becomes a smaller fraction of the ensemble mean value, implying greater agreement among models and statistical significance of the ensemble mean value. To reduce uncertainty, values with $|CV| > 0.8$ are not considered, corresponding approximately to an average agreement of four out of five models (i.e., 80% probability).

Finally, WEF or UCHrisk variation induced by climate change is assessed by means of absolute changes ($\Delta\alpha$) for each period (mid-century and end-of-century periods) corresponding to the RCP 4.5 and RCP 8.5 scenarios (α_{RCP}) with respect to baseline values ($\alpha_{baseline}$):

$$\Delta\alpha = \alpha_{RCP} - \alpha_{baseline} \quad (4)$$

3. Results

3.1. Wave Climate

3.1.1. EQM Correction

Global wave model outputs, with and without correction, were compared with corrected Med-WAV (Figure 3). The uncorrected global models underestimate significant wave height (Hs) values and extreme Hs values. This is particularly noticeable for ACCESS 1.0, GFDL-ESM2G, and GFDL-ESM2M (Figure 3A,D,E; also, see Table S1 in SM) where the EQM largely improves the Hs NBI index. CSIRO-Mk3.6.0 and EC-EARTH show better performance (HH ~0.8; Table S1 in SM) with an EQM improvement of ~5% in HH.

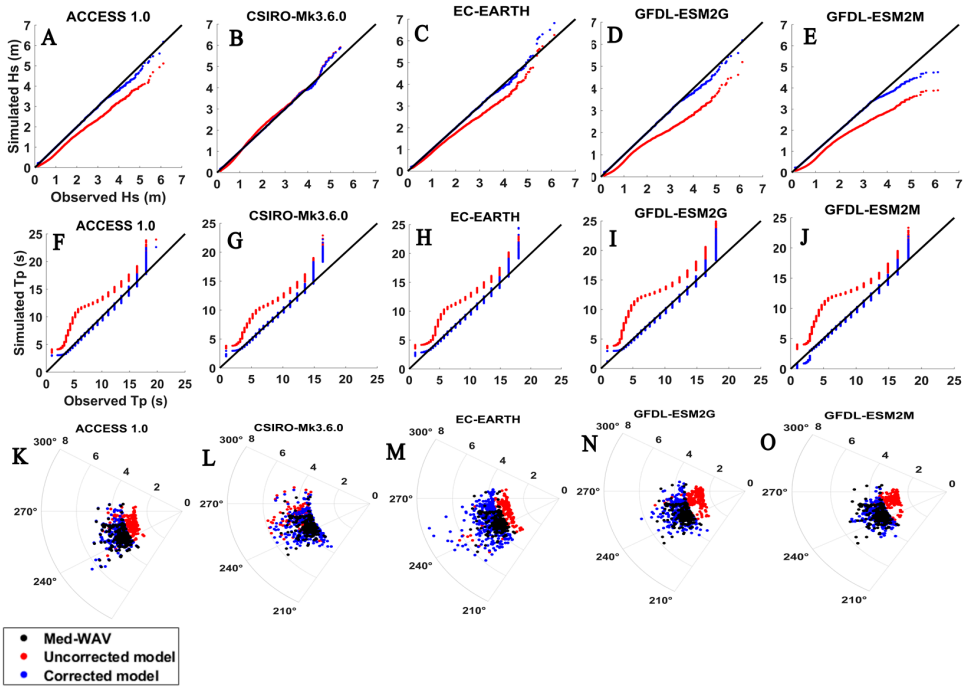

Figure 3. Q-Q plot of significant wave height (Hs) (**A**–**E**) peak period (Tp) (**F**–**J**). Polar plot for wave heights exceeding 99th percentile (**K**–**O**). Uncorrected global wave model (red), corrected global wave model (blue), and Med-WAV reanalysis (black) are represented.

The uncorrected global wave model outputs overestimate, in general, the peak period (Tp) (NRMSE ~0.6), with EQM correction improving ~10% for CSIRO-Mk3.6.0 and EC-EARTH models (Figure 3G,H) and ~18% for the rest of the models (Figure 3F,I,J).

For the case of wave directions with an Hs greater than or equal to the 99th percentile (P99), the uncorrected models show a deviation of approximately 25° ($NRMSE_\theta$ ~39°; Figure 3K,L,N,O). After applying the EQM correction, this improves by 63% ($NRMSE_\theta$ ~ 20°), except for the case of EC-EARTH, where the bias increases by 66% (Figure 3M). Overall, in the study area, EC-EARTH and CSIRO-Mk3.6.0 show the best agreement with the Med-WAV reanalysis, both with and without correction. Specifically, CSIRO shows better alignment for Hs, especially for extreme values. On the other hand, EC-EARTH performs better in capturing extreme Tp values compared to the other models. Regarding wave direction, EC-EARTH

shows the best agreement among the uncorrected models. However, after applying the EQM correction, CSIRO achieves the most accurate alignment with the observed data.

3.1.2. The Validation of the Wave Propagation Method

This section summarizes the performance of the wave propagation method to reproduce average and extreme wave conditions (>99th). This step is crucial for reducing the uncertainties associated with global models, which do not accurately represent wave transformation processes in intermediate and shallow waters due to their limited spatial resolution. Due to the lack of observational data within the bay, SIMAR points were selected to assess the model's performance within the bay. SIMAR reanalysis was selected as the best alternative due to its wide spatial distribution in the region, good temporal coverage, and frequent use in wave studies conducted across the Iberian Peninsula (e.g., [56,57]). Table 5 shows the average values of skill scores for Hs, Tp, and Dir calculated in the eight SIMAR locations in the Bay of Cadiz. The validation indicates a good performance, especially for extreme wave conditions, for Hs (ro = 0.95; HH = 0.07) and Tp (ro = 0.82; HH = 0.18). The biases related to Hs are practically zero, while Tp is generally affected by a negative bias. However, the results are quite adequate. The wave direction shows also good agreement, although performance worsens in extreme events.

Table 5. Statistical scores for mean and extreme significant wave height, peak period, and mean direction between propagated series and SIMAR points.

	ro	HH	NRMSE	NBI
Hs (m)	0.96	0.18	0.18	0.05
P99 Hs	0.95	0.07	0.07	−0.02
Tp (s)	0.82	0.28	0.26	−0.14
P99 Tp (s)	0.83	0.18	0.17	−0.11
Dir (°)	-	-	2.60	−1.72
P99 Dir (°)	-	-	13.42	38.39

3.2. Changes in WEF

Scalar and Direction Climate

The WEF associated with a 10-year return period (RT10) shows maxima (around 15×10^4 Wm^{-1}) in the outer domain and by the rocky outcrops outside the bay. Minima appear by the coast, where shallow depths and the wave breaking limit reduce the WEF, and inside the bay due to the protective effect of the Cadiz tombolo against wave front propagation (Figure 4A). Under RCP4.5, the WEF associated with RT10 shows a general decrease, slightly increasing only by some coastal stretches, over rocky outcrops and inside the bay (Figure 4B,C). The general WEF decrease is weaker in the end-of-century period than in the mid-century period as a result of the larger SLR. The mid-century RCP8.5 WEF change pattern replicates that of the RCP4.5 WEF, but with a weaker general decrease and slightly larger increments located in the shallower areas (Figure 4E). By the end-of-century period in RCP8.5, there is a general WEF increase, with maxima located at shallow waters and rocky outcrops (Figure 4F). Additionally, a southward shift in the WEF direction is evident in all cases except for RCP4.5 in the mid-future period.

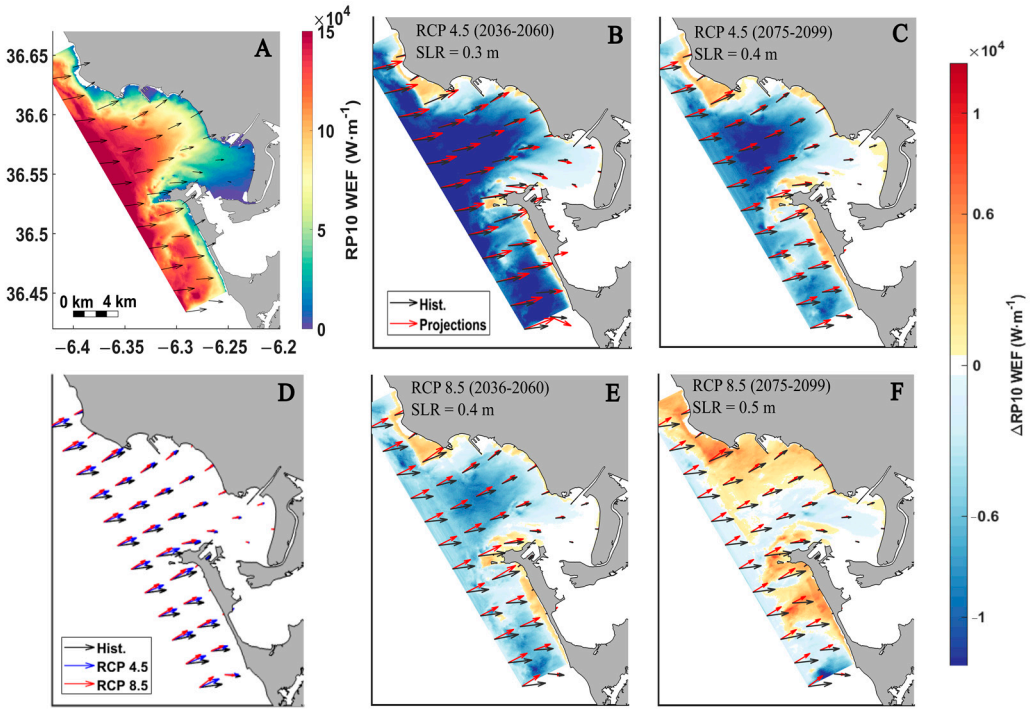

Figure 4. (**A**) The wave energy flux corresponding to the 10-year return period and the mean direction associated with the 99th percentile or greater of the WEF (black arrow). The absolute change and mean direction associated with the 99th percentile of the WEF for each simulation (red arrow): (**B**) the 2036–2060 period of the RCP 4.5 scenario, (**C**) the 2075–2099 period of the RCP 4.5 scenario, (**E**) the 2036–2060 period of the RCP 8.5 scenario, and (**F**) the 2075–2099 period of the RCP 8.5 scenario. The sea level rise (SLR) for each period is shown in the bottom left corner and represents the average increase calculated from the five global models used. (**D**) The mean direction associated with the 99th percentile or greater of the WEF for the historical period (black arrow), the end-of-century period of the RCP 4.5 scenario (blue arrow), and the end-of-century period of the RCP 8.5 scenario (red arrow).

Such a direction shift also takes place for the most energetic waves. Figure 4D shows the average of the directions of the extreme waves (>99th) for the historical period and for the end-of-century period in the RCP 4.5 and RCP 8.5 scenarios. While the most energetic waves impact the bay from the west (ca. 263°) during the historical period, they come from 250° in the RCP 4.5 scenario and from 240° in RCP 8.5. This change in the direction of incident waves in the bay leads to an alteration in their propagation within the Bay of Cadiz, resulting in a greater impact on the areas of Rota, Cadiz, and the surrounding areas.

To determine how the increase in sea level affects wave propagation, the methodology is repeated without considering the SLR (Figure 5). These results show a larger WEF decrease than when considering SLR, which is particularly notable over the shallow coastal areas and rocky outcrops, where the depth increase due to SLR makes a substantial contribution to the WEF.

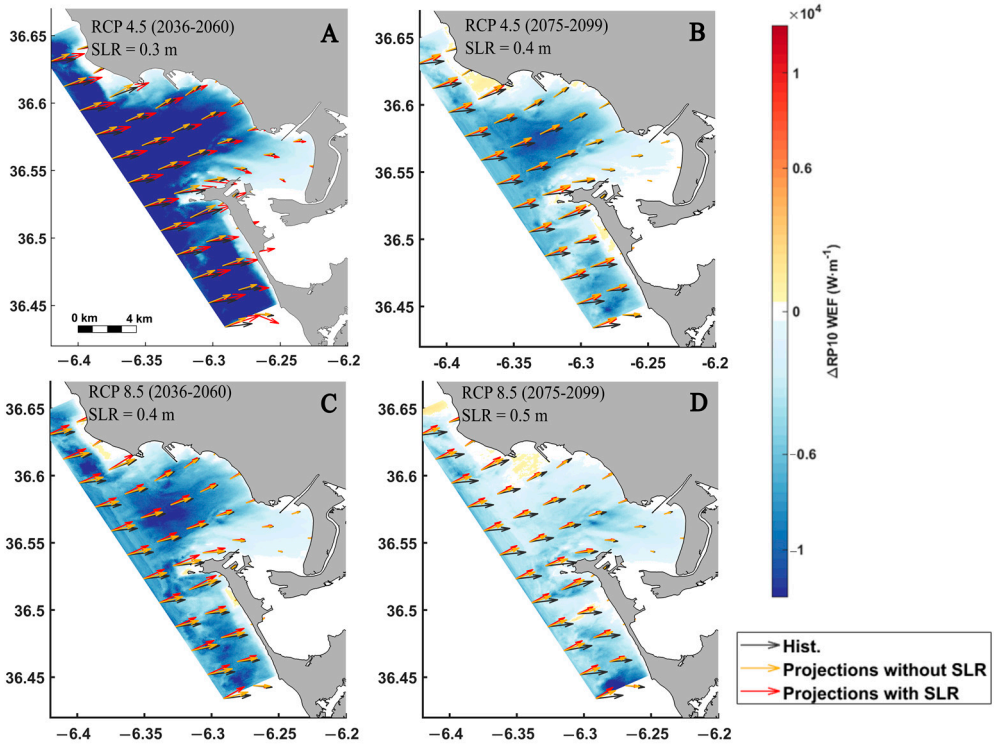

Figure 5. The absolute changes in wave energy flux (WEF) with and without sea level rise are shown for the following: (**A**) the 2036–2060 period of the RCP 4.5 scenario, (**B**) the 2075–2099 period of the RCP 4.5 scenario, (**C**) the 2036–2060 period of the RCP8.5 scenario, and (**D**) the 2075–2099 period of the RCP 8.5 scenario. The mean direction associated with the 99th percentile or greater of the WEF for the historical period (black arrow) is shown with sea level rise (red arrow) and without SLR (orange arrow) projections.

3.3. Hazard Assessment

3.3.1. Decontextualization Hazard

We relate decontextualization hazard (DCR) to the maximum critical diameter of an object (we assume sphericity) susceptible to be displaced due to wave action over a 10-year return period (Figure 6). All projections present a slight general reduction in the value of DCR, except for the bay's interior and shallower areas, where local significant increases (up to 25%) are observed compared to the historical period. This result aligns with the projected general reduction in the WEF and its local increase in shallower areas. In shallow areas, the wave-induced bottom stress is larger, but as wave orbital velocity strongly attenuates with an increasing depth (Figure S1), DCR is reduced throughout the rest of the bay. The mid-century RCP4.5 and the end-of-century RCP8.5 scenarios exhibit the most substantial hazard changes. However, the result of these changes reflects only as a decrease in the bay area under a hazard score of 3 and an increase in the bay area as a hazard score of 2. The percentages of the bay area classified as high and very high hazards (scores of 4 and 5; Figure 6D) remain nearly unchanged.

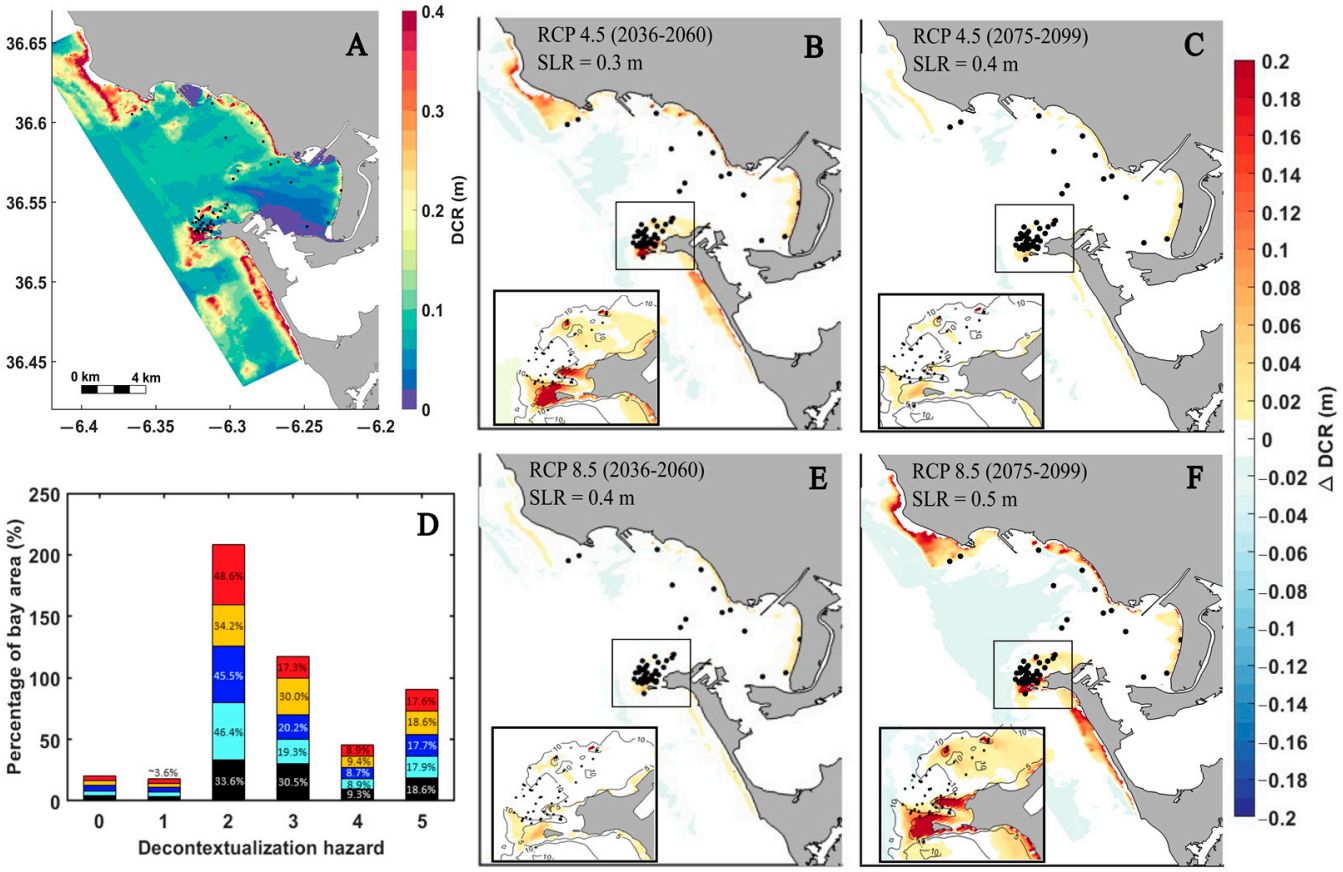

Figure 6. (**A**) A map of decontextualization hazard (the critical diameter of an object moved under wave action) for the historical period. The absolute change in this hazard for (**B**) the 2036–2060 period of the RCP 4.5 scenario, (**C**) the 2075–2099 period of the RCP 4.5 scenario, (**E**) the 2036–2060 period of the RCP 8.5 scenario, and (**F**) the 2075–2099 period of the RCP 8.5 scenario compared with the historical period. The black points indicate the locations of UCH sites. (**D**) A histogram of the hazard at UCH sites and hazard classes. The sea level rise (SLR) for each period is shown in the bottom left corner and represents the average increase calculated from the five global models used.

3.3.2. Scour Hazard

The scour hazard indicator is represented by the potential volume of scouring corresponding to a 10-year return period (Figure 7). In general, no significant changes in the scouring hazard are observed in the Bay of Cadiz for all the scenarios and periods considered. However, locally significant variations are identified in the shallower areas of the bay (less than 5 m) and in some rocky outcrops, such as those located off Rota and Cadiz. In these areas, the RCP 4.5 scenario for the mid-century period and the RCP 8.5 scenario for the end-of-century period show mostly positive anomalies, while the RCP 4.5 scenario for the end-of-century period and the RCP 8.5 scenario for the mid-century period exhibit mostly negative anomalies. These changes result in an increase in the percentage of the bay area classified as a high hazard level (4), accompanied by a decrease in the very high hazard level (5; Figure 7D). The percentage change is very similar across all periods; however, it is at the end of the century for the RCP 4.5 scenario where the greatest reduction in the percentage of the bay area classified as having a very high hazard level is observed.

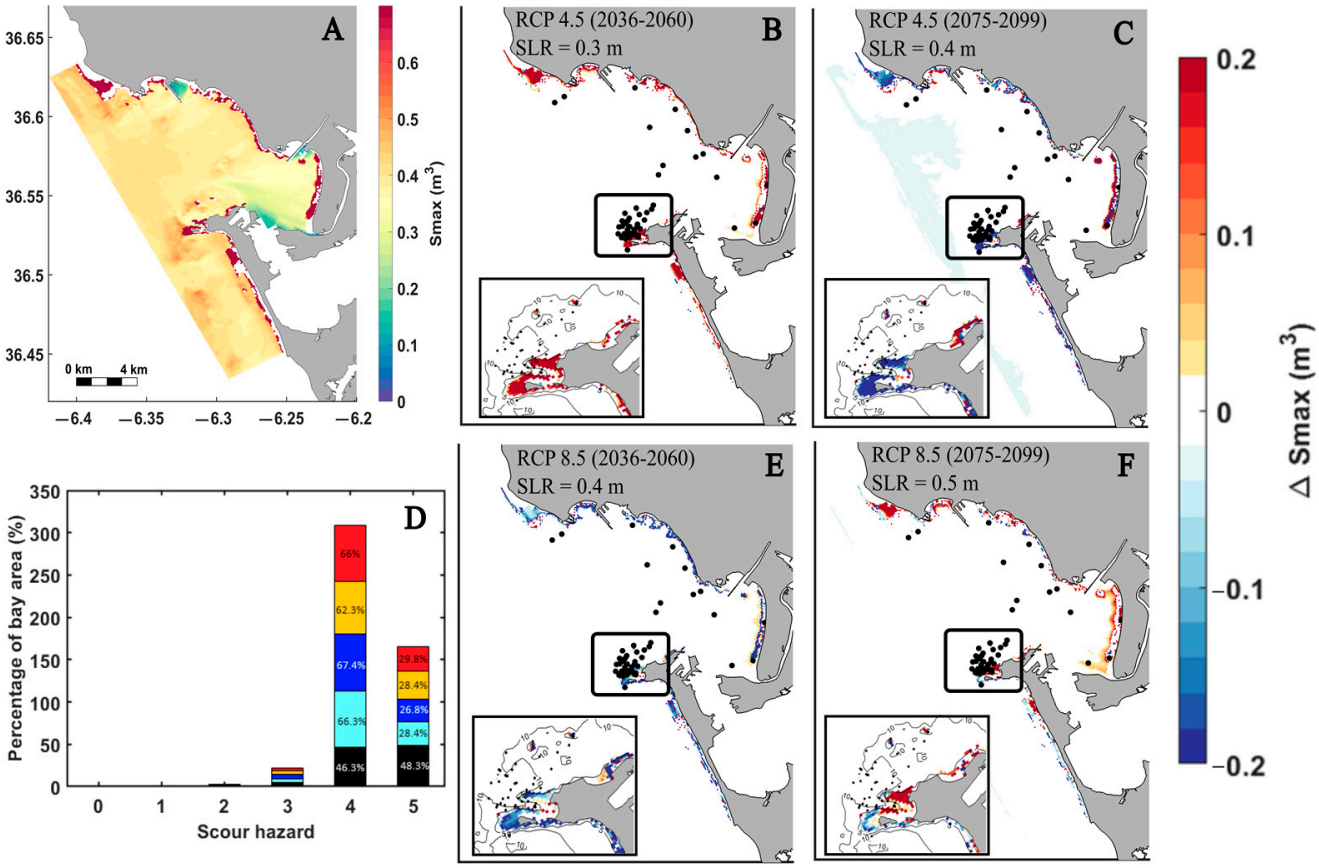

Figure 7. (**A**) A map of the scour hazard (scour volume) for the historical period. The absolute change in this hazard for (**B**) the 2036–2060 period of the RCP 4.5 scenario, (**C**) the 2075–2099 period of the RCP 4.5 scenario, (**E**) the 2036–2060 period of the RCP 8.5 scenario, and (**F**) the 2075–2099 period of the RCP 8.5 scenario compared with the historical period. The black points indicate the locations of UCH sites. (**D**) A histogram of the hazard at UCH sites and hazard classes. The sea level rise (SLR) for each period is shown in the bottom left corner and represents the average increase calculated from the five global models used.

3.3.3. Wear Erosion Hazard

The indicator erosive wear hazard is analyzed by means of the erosion potential (Figure 8). This hazard exhibits the most significant future changes compared to the historical period. The changes for both scenarios are predominantly positive, indicating an increase in the magnitude of the hazard. These changes are more intense near the southern entrance of the bay, where most UCH sites are located. However, significant negative anomalies are also recorded at the rocky outcrops off the city of Cadiz, being more pronounced in the RCP 8.5 scenario, particularly towards the end of the century. As a result, there is an increase in the percentage of the bay area that will be affected by a very high hazard level (5) for erosive wear hazard (Figure 8D).

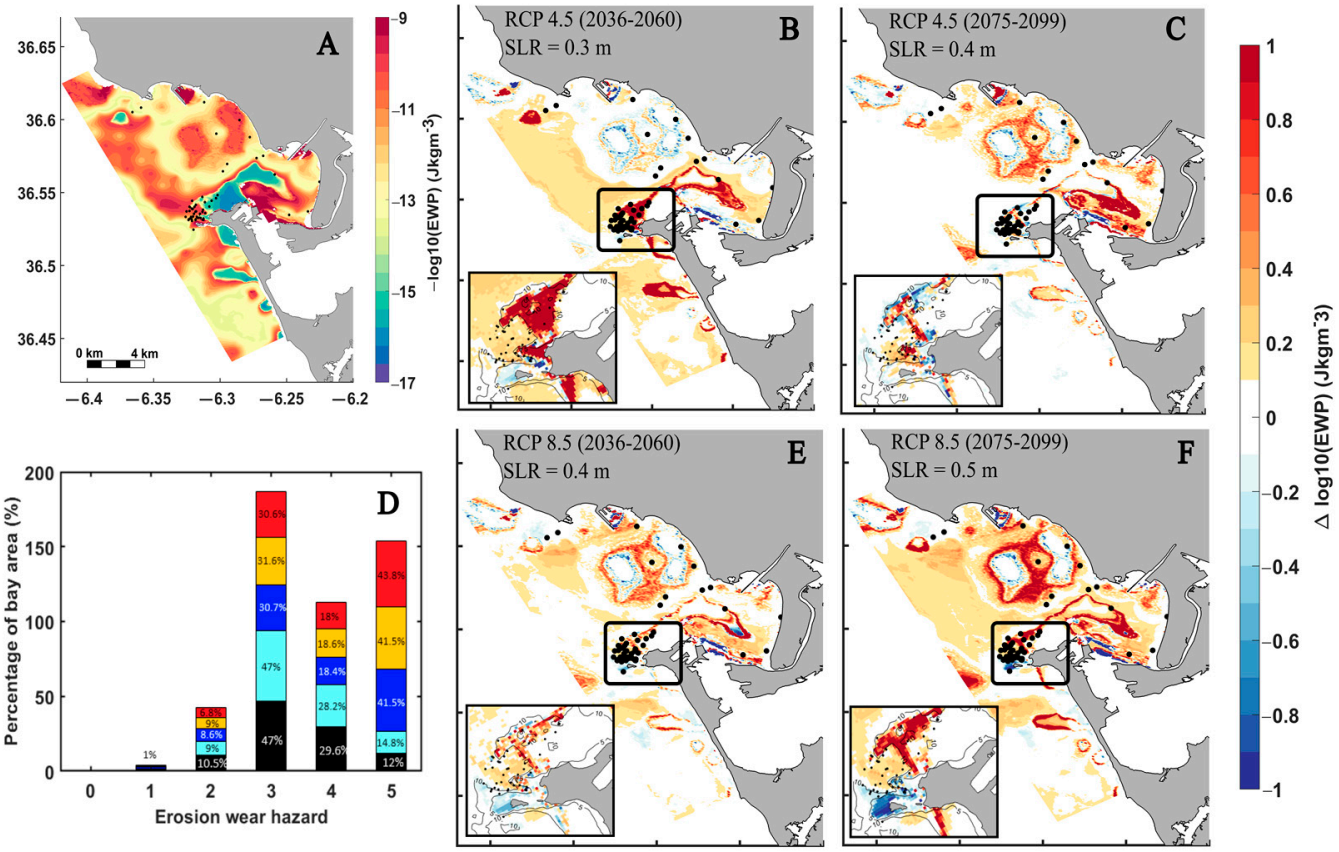

Figure 8. (**A**) A map of the erosive wear hazard (log of erosive wear potential) for the historical period. The absolute change in this hazard for (**B**) the 2036–2060 period of the RCP 4.5 scenario, (**C**) the 2075–2099 period of the RCP 4.5 scenario, (**E**) the 2036–2060 period of the RCP 8.5 scenario, and (**F**) the 2075–2099 period of the RCP 8.5 scenario compared with the historical period. The black points indicate the locations of UCH sites. (**D**) A histogram of the hazard at UCH sites and hazard classes. The sea level rise (SLR) for each period is shown in the bottom left corner and represents the average increase calculated from the five global models used.

3.4. UCH Risk Assessment

Figure 9 shows the underwater cultural heritage risks (UCHRs) at the studied sites in the Bay of Cadiz. During the historical period, there are 7 UCH sites under decontextualization risk, 19 under scour risk, and 21 under wear erosion risk ($UCHR_{DE}$, $UCHR_{SC}$, and $UCHR_{EW} > 3.2$). The sites under risk are mainly located around the city of Cadiz, with the exception of two located by the eastern coast of the Bay of Cadiz (Valdelagrana). In general, the sites present lower risk values associated with decontextualization and larger risk values associated with erosion wear. In the historical period, the distribution of risks is skewed towards low values for $UCHR_{DE}$, centered near 3.2 for UCH_{SC}, and it presents a bimodal distribution with a narrow peak at 3.8 for UCH_{WE}. In the future scenarios, the number of UCH sites at risk (>3.2) remains unchanged for the risks of decontextualization and scouring. However, for wear erosion under the RCP 4.5 scenario, the number of sites at risk increases from 21 to 23 at the mid-century period and to 22 at the end of the century (Figure 10). The sites turning under risk are located at the rocky outcrops off the city of Cadiz and are related to strong and very local changes in erosion wear hazard (see Figure 8).

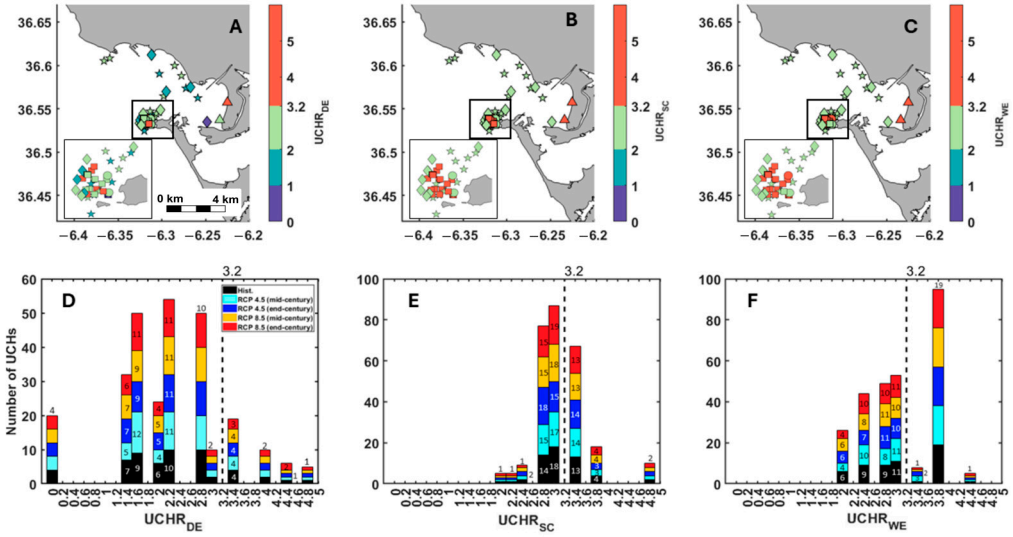

Figure 9. (**A**) The decontextualization risk ($UCHR_{DE}$) for UCH sites located in the Bay of Cadiz, (**B**) the scour risk ($UCHR_{SC}$) for UCH sites, and (**C**) the wear erosion risk ($UCHR_{EW}$) for UCH sites. Warm colors indicate a higher risk index, and different shapes refer to the prevalent material (diamonds, metallic material; squares, ceramic material; filled circles, stone; triangles, wood/organic material; pentagons, unknown material). Accumulated graphs of the classification of UCHs in terms of the risks of (**D**) decontextualization, (**E**) scour, and (**F**) wear erosion.

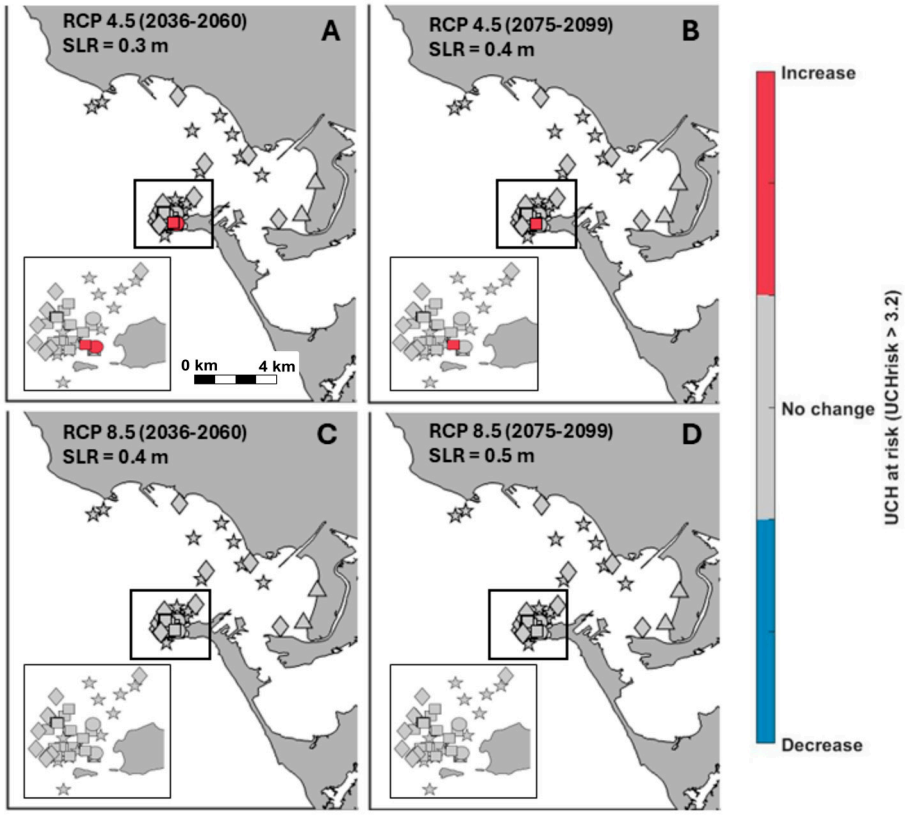

Figure 10. The erosive wear risk ($UCHR_{EW}$) for UCH sites located in the Bay of Cadiz. The absolute change for (**A**) the 2036–2060 period of the RCP 4.5 scenario, (**B**) the 2075–2099 period of the RCP 4.5 scenario, (**C**) the 2036–2060 period of the RCP 8.5 scenario, and (**D**) the 2075–2099 period of the RCP 8.5 scenario compared with the historical period. The sea level rise (SLR) for each period is shown in the bottom left corner and represents the average increase calculated from the five global models used.

4. Discussion

This study outlines a methodology to evaluate the impacts of climate change on UCH through wave-induced hazards. It is based on a hybrid downscaling [33] of the bias-corrected wave fields [31,32] corresponding to the CMIP5 RCP4.5 and RCP8.5 scenarios. Both scenarios show a robust reduction in significant wave height in the North Atlantic (see also Wang et al. [58] and Lemos et al. [59]). However, most UCH is placed in shallow coastal areas, where the wave fields will be affected by shallow water processes, coastline orientation and bathymetric relief, and by the concurrent SLR; therefore, downscaling the global wave fields is necessary. Our results show that the use of the EQM method and the directional adjustment improved the global wave model outputs (see Table S1). This correction is key for obtaining accurate high-resolution wave propagated fields. This is corroborated by the validation of the wave downscaled fields against SIMAR reanalysis points (Table 3). The validation presented very good results for both mean wave climate and for extreme P99 waves.

Changes in the future WEF are the result of the combination of changes in projected significant wave height, energy (~peak) period, and depth changes (Equation (2)). As changes in peak period are small, the resulting WEF changes result from the opposite contribution of significant wave height diminution and sea level rise. The result is a general reduction in the WEF in the Bay of Cadiz, with local increases in shallow rocky outcrops and coastal areas, where the depth increase by SLR allows for the higher waves to appear without breaking. These results are consistent with the findings of Aarns et al. [25] and Chaigneau et al. [28], who demonstrated that changes in depth induced by sea level rise can lead to higher wave amplitudes near the coast. The impact of sea level variations is substantially more important on extreme significant wave heights over the wide continental shelf where shallow water dynamics prevail, particularly in large tidal range areas [28]. However, our results show the important contribution of SLR to changes in the WEF in a mesotidal bay (see Figure 5). This demonstrates that accurate high-resolution wave propagation fields enable better capture of the nonlinear interactions between sea level and waves. Additionally, there is a shift in the direction of incident waves, increasing the wave exposure in certain areas of Cadiz and Rota. Along with these changes in the WEF, there is a reduction in wave orbital velocity (Figure S1; increased depth and decreased Hs), which is a fundamental parameter for UCH risk assessment, either by direct impact of orbital velocity on object decontextualization or scour and wear erosion impact.

Our assessment of the impact of wave climate changes on UCH hazards shows limited consequences. For decontextualization and scour hazard, the changes in the critical diameter of the moved object and in scour volume are, in general, small. There are considerable changes only in those locations (shallows and coastal areas), where the hazard indicators already had maximum values and had very high hazard levels (>0.16 m and > 0.4 m^3 for decontextualization and scour indicators, respectively (Table 3; Fernández-Montblanc et al. [7])). Therefore, it is not surprising that remarkable increases, such as the 0.2 m increase in the decontextualization hazard indicator, have no clear impact on the distribution of hazard levels within the bay. Indeed, there is a strong sensitivity of the hazard change assessment to the definition of the hazard level classes.

Hazard and vulnerability thresholds are mainly determined through the likelihood of exceeding certain predefined thresholds [60] and active participation from local users and stakeholders responsible for the management and conservation of cultural heritage [61,62]. The reliance on hazard categories based on historical data assumes that future conditions will follow probability distributions similar to those of the past. However, climate change is significantly altering these distributions, increasing the frequency and intensity of extreme events, which shifts hazard thresholds toward higher categories. This could explain

why there are not important changes in UCH risk under the considered climate change scenarios; however, this does not imply that such changes are not occurring. The lack of quantitative data on observed and projected impacts under different climate scenarios limits the ability to establish acceptable risk thresholds and develop effective adaptation and mitigation strategies [63].

The proposed methodology represents the first attempt, to our knowledge, for addressing UCH risk assessment for wave-induced hazards under climate change projections, and it is not free of shortcomings and limitations. Some of the methodological limitations related to the simplifications applied to hazard quantification are exposed in [7]. Here, it is necessary to add the assumption used in the EQ bias correction that the wave parameter distributions (period, height, and direction) will remain unchanged in the future. Clearly, this may not be the case in real life, but it is the simplest and best choice we have. It is important to note that our study did not include the contribution of storm surge to the water level, as it was initially omitted due to the predominant influence of tides on the total water level in the study area. Additionally, the lack of consideration for possible changes in morphodynamic processes, such as those related to depth and the interaction between waves and currents, represents a significant limitation in our analysis. It is crucial to recognize that the relative rise in sea level could be mitigated by sediment accommodation depending on the sediment budget, which would have a substantial impact on coastal dynamics. Furthermore, the impact of waves on sea level was not included; if this factor was incorporated into the ocean model, it would result in a higher sea level, which, in turn, would have a greater effect on wave propagation and the hazards affecting underwater cultural heritage. For future research, it would be valuable to conduct a multiple-hazard analysis to assess whether risky events occur simultaneously in a cascading or cumulative manner over time. In risk assessment studies, multidisciplinary approaches and the use of precise data are of utmost importance for managing the impacts of climate change in coastal contexts [64]. Furthermore, the proposed methodology must be expanded to other environmental factors influencing UCH preservation (i.e., water temperature, salinity, and pH) to provide a holistic methodology to assess the evolution of the natural hazards affecting the in situ preservation of UCH in the context of CC.

5. Conclusions

Future changes in sea levels and wave climate in coastal areas represent one of the major threats to the preservation and conservation of underwater cultural heritage (UCH). However, understanding how these changes will unfold in the long term and the associated hazards remains a challenge due to the complexity and interaction between the processes involved. In this study, we propose an innovative methodology to assess the risk to UCH in shallow waters based on hybrid downscaling using an ensemble derived from CMIP5 wave projections. This methodology applies downscaling to bias-corrected wave fields corresponding to the RCP4.5 and RCP8.5 scenarios from CMIP5. The approach focuses on the primary wave-induced hazards, considering their impact on the long-term preservation of UCH: archeological decontextualization, scouring, and wear erosion. To evaluate the effects of climate change, we compare the historical period (1981–2005) with two future periods, the mid-century (2036–2060) and end-of-century (2075–2099) periods, for both scenarios.

First, we present and validate the methodology for wave correction and propagation. Our results show that the use of the EQM method and directional adjustment improved the global wave model outputs, which is essential for obtaining high-resolution and accurate propagated wave fields. Second, we assessed changes in wave climate, observing a general reduction in the wave energy flux in the Bay of Cadiz, with local increases in rocky outcrops

and coastal areas, where the increased depth due to SLR allows higher waves to appear without breaking. This finding highlights the importance of high-resolution wave fields in capturing the nonlinear interactions between sea level and waves. Additionally, a shift in the direction of incident waves was identified, increasing wave exposure in certain areas of Cadiz and Rota.

In the bay, a general reduction in wave orbital velocity is observed due to increased depth and decreased significant wave height. This parameter is crucial for assessing UCH risk, as most UCH sites lie on the seafloor. However, in shallow areas, where the highest density of UCH is concentrated, significant changes in decontextualization and scouring hazards are observed. The only relevant changes in risk (UCHrisk > 3.2) are associated with wear erosion, particularly in the sites located on rocky outcrops off the city of Cadiz, where local changes in this hazard are marked. However, the strict definitions of hazard level classes, which shift thresholds toward higher categories, do not adequately reflect the changes in hazard classes. This factor could explain why significant changes in UCH risk are not observed under the considered climate change scenarios, although this does not imply that such changes are not occurring.

In conclusion, this study emphasizes the importance of conducting local-scale studies that incorporate the nonlinear interactions between sea level and waves in extreme wave studies, as these interactions could lead to local trends in wave energy that are different to those indicated in the global projections. This could result in variations in the impact on UCH risk in specific areas. It is also crucial to consider the high sensitivity in defining hazard level classes, as inadequate definitions may mask significant changes in UCH risk. The obtained results offer the possibility to iteratively redefine the hazard level and/or hazard classes accounting for future changes. The proposed methodology offers a tool to perform a quantitative analysis on the impact of CC on UCH rather than the existing state-of-the-art qualitative approach and method. The methodology developed in this study therefore represents a crucial step toward a more accurate understanding and more effective management of UCH risk in the face of climate change, an area that has been relatively overlooked until now. This tool provides innovative approaches for decision making in the protection and conservation of this invaluable heritage.

Supplementary Materials: The following supporting information can be downloaded at https://www.mdpi.com/article/10.3390/jmse13010136/s1.

Author Contributions: Conceptualization, C.F.-M., A.I. and T.F.-M.; methodology, C.F.-M., A.I. and T.F.-M.; software, C.F.-M., A.I. and T.F.-M.; validation, C.F.-M., A.I. and T.F.-M.; formal analysis, C.F.-M., A.I. and T.F.-M.; investigation, C.F.-M., A.I. and T.F.-M.; resources, C.F.-M., A.I., M.B. and T.F.-M.; data curation, C.F.-M., A.I. and T.F.-M.; writing—original draft preparation, C.F.-M.; writing—review and editing, C.F.-M., A.I., M.B. and T.F.-M.; visualization, C.F.-M.; supervision, A.I. and T.F.-M.; project administration, M.B. and T.F.-M.; funding acquisition, M.B. and T.F.-M. All authors have read and agreed to the published version of the manuscript.

Funding: This study was partially supported by the Ministry of Science and Innovation thorough the project "Vulnerability of littoral cultural heritage to environmental agents: impact of climate change (VOLICHE)" (PID2020-117812RB-I00/AEI/10.13039/501100011033).

Institutional Review Board Statement: Not applicable.

Informed Consent Statement: Not applicable.

Data Availability Statement: The raw data supporting the conclusions of this article will be made available by the authors, without undue reservation.

Acknowledgments: The authors acknowledge Lorenzo Mentaschi for his useful suggestions and for providing the global wave projection dataset used in this study.

Conflicts of Interest: The authors declare no conflicts of interest.

References

1. Thiébot, J.; Idier, D.; Garnier, R.; Falqués, A.; Ruessink, B.G. The Influence of Wave Direction on the Morphological Response of a Double Sandbar System. *Cont. Shelf Res.* **2012**, *32*, 71–85. [CrossRef]
2. Pérez-Reverte Mañas, C.; Cerezo Andreo, F.; López Osorio, P.; González Gallero, R.; Mariscal Rico, L.; Arévalo González, A. Underwater Cultural Heritage as an Engine for Social, Economic and Cultural Development. State of Research at the University of Cadiz (Andalusia, Spain). *Heritage* **2021**, *4*, 2676–2690. [CrossRef]
3. Khakzad, S.; Pieters, M.; Van Balen, K. Coastal Cultural Heritage: A Resource to Be Included in Integrated Coastal Zone Management. *Ocean Coast. Manag.* **2015**, *118*, 110–128. [CrossRef]
4. Potts, A.L.A. *European Cultural Heritage Green Paper*; Europa Nostra: The Hague, The Netherlands; Brussels, Belgium, 2021.
5. Quinn, R. The Role of Scour in Shipwreck Site Formation Processes and the Preservation of Wreck-Associated Scour Signatures in the Sedimentary Record—Evidence from Seabed and Sub-Surface Data. *J. Archaeol. Sci.* **2006**, *33*, 1419–1432. [CrossRef]
6. Fernández-Montblanc, T.; Quinn, R.; Izquierdo, A.; Bethencourt, M. Evolution of a Shallow Water Wave-Dominated Shipwreck Site: Fougueux (1805), Gulf of Cadiz. *Geoarchaeology* **2016**, *31*, 487–505. [CrossRef]
7. Fernández-Montblanc, T.; Bethencourt, M.; Izquierdo, A. Underwater Cultural Heritage Risk Assessment Methodology for Wave-Induced Hazards: The Showcase of the Bay of Cadiz. *Front. Mar. Sci.* **2022**, *9*, 1005514. [CrossRef]
8. Fernández-Montblanc, T.; Izquierdo, A.; Quinn, R.; Bethencourt, M. Waves and Wrecks: A Computational Fluid Dynamic Study in an Underwater Archaeological Site. *Ocean Eng.* **2018**, *163*, 232–250. [CrossRef]
9. McNinch, J.E.; Wells, J.T.; Trembanis, A.C. Predicting the Fate of Artefacts in Energetic, Shallow Marine Environments: An Approach to Site Management. *Int. J. Naut. Archaeol.* **2006**, *35*, 290–309. [CrossRef]
10. Astley, A.J. The Taphonomy of Historic Shipwreck Sites. Ph.D. Thesis, University of Southampton, Southampton, UK, 2016.
11. Bates, C.R.; Lawrence, M.; Dean, M. Robertson Geophysical Methods for Wreck-Site Monitoring: The Rapid Archaeological Site Surveying and Evaluation (RASSE) Programme. *Int. J. Naut. Archaeol.* **2011**, *40*, 404–416. [CrossRef]
12. Quinn, R.; Smyth, T.A.G. Processes and Patterns of Flow, Erosion, and Deposition at Shipwreck Sites: A Computational Fluid Dynamic Simulation. *Archaeol. Anthropol. Sci.* **2018**, *10*, 1429–1442. [CrossRef]
13. Plets, R.; Quinn, R.; Forsythe, W.; Westley, K.; Bell, T.; Benetti, S.; McGrath, F.; Robinson, R. Robinson Using Multibeam Echo-Sounder Data to Identify Shipwreck Sites: Archaeological Assessment of the Joint Irish Bathymetric Survey Data. *Int. J. Naut. Archaeol.* **2011**, *40*, 87–98. [CrossRef]
14. Bethencourt, M.; Fernández-Montblanc, T.; Izquierdo, A.; González-Duarte, M.M.; Muñoz-Mas, C. Study of the Influence of Physical, Chemical and Biological Conditions That Influence the Deterioration and Protection of Underwater Cultural Heritage. *Sci. Total Environ.* **2018**, *613–614*, 98–114. [CrossRef] [PubMed]
15. Angelini, E.; Grassini, S.; Tusa, S. Underwater Corrosion of Metallic Heritage Artefacts. In *Corrosion and Conservation of Cultural Heritage Metallic Artefacts*; Woodhead Publishing: Cambridge, UK, 2013; pp. 236–259. [CrossRef]
16. Cámara, B.; De Buergo, M.Á.; Bethencourt, M.; Fernández-Montblanc, T.; La Russa, M.F.; Ricca, M.; Fort, R. Biodeterioration of Marble in an Underwater Environment. *Sci. Total Environ.* **2017**, *609*, 109–122. [CrossRef]
17. Björdal, C.G.; Nilsson, T. Reburial of Shipwrecks in Marine Sediments: A Long-Term Study on Wood Degradation. *J. Archaeol. Sci.* **2008**, *35*, 862–872. [CrossRef]
18. Alexandrakis, G.; Petrakis, S.; Kampanis, N. Preliminary Assessment of Wave Energy Hazards in a Shallow Underwater Cultural Heritage Site. In Proceedings of the 2023 IMEKO TC-4 International Conference on Metrology for Archaeology and Cultural Heritage, Rome, Italy, 19–21 October 2023.
19. Weisse, R.; von Storch, H. *Marine Climate and Climate Change, Storms, Wind Waves and Storm Surges*; Praxis Publishing: Chichester, UK, 2010.
20. Reguero, B.G.; Losada, I.J.; Méndez, F.J. A Recent Increase in Global Wave Power as a Consequence of Oceanic Warming. *Nat. Commun.* **2019**, *10*, 205. [CrossRef]
21. Casas-Prat, M.; Wang, X.L.; Swart, N. CMIP5-Based Global Wave Climate Projections Including the Entire Arctic Ocean. *Ocean Model.* **2018**, *123*, 66–85. [CrossRef]
22. Hemer, M.A.; Fan, Y.; Mori, N.; Semedo, A.; Wang, X.L. Projected Changes in Wave Climate from a Multi-Model Ensemble. *Nat. Clim. Change* **2013**, *3*, 471–476. [CrossRef]
23. Mentaschi, L.; Vousdoukas, M.I.; Voukouvalas, E.; Dosio, A.; Feyen, L. Global Changes of Extreme Coastal Wave Energy Fluxes Triggered by Intensified Teleconnection Patterns. *Geophys. Res. Lett.* **2017**, *44*, 2416–2426. [CrossRef]
24. Morim, J.; Hemer, M.; Wang, X.L.; Cartwright, N.; Trenham, C.; Semedo, A.; Young, I.; Bricheno, L.; Camus, P.; Casas-Prat, M.; et al. Robustness and Uncertainties in Global Multivariate Wind-Wave Climate Projections. *Nat. Clim. Change* **2019**, *9*, 711–718. [CrossRef]

25. Aarnes, O.J.; Reistad, M.; Breivik, Ø.; Bitner-Gregersen, E.; Ingolf Eide, L.; Gramstad, O.; Magnusson, A.K.; Natvig, B.; Vanem, E. Projected Changes in Significant Wave Height toward the End of the 21st Century: Northeast A Tlantic. *J. Geophys. Res. Ocean.* **2017**, *122*, 3394–3403. [CrossRef]
26. Morim, J.; Vitousek, S.; Hemer, M.; Reguero, B.; Erikson, L.; Casas-Prat, M.; Wang, X.L.; Semedo, A.; Mori, N.; Shimura, T.; et al. Global-Scale Changes to Extreme Ocean Wave Events Due to Anthropogenic Warming. *Environ. Res. Lett.* **2021**, *16*, 074056. [CrossRef]
27. Meucci, A.; Young, I.R.; Hemer, M.; Kirezci, E.; Ranasinghe, R. Projected 21st Century Changes in Extreme Wind-Wave Events. *Sci. Adv.* **2020**, *6*, eaaz7295. [CrossRef] [PubMed]
28. Chaigneau, A.A.; Law-Chune, S.; Melet, A.; Voldoire, A.; Reffray, G.; Aouf, L. Impact of Sea Level Changes on Future Wave Conditions along the Coasts of Western Europe. *Ocean Sci.* **2023**, *19*, 1123–1143. [CrossRef]
29. Alvarez, O.; Izquierdo, A.; Tejedor, B.; Mañanes, R.; Tejedor, L.; Kagan, B.A. The Influence of Sediment Load on Tidal Dynamics, a Case Study: Cádiz Bay. *Estuar. Coast. Shelf Sci.* **1999**, *48*, 439–450. [CrossRef]
30. Kagan, B.A.; Tejedor, L.; Álvarez, O.; Izquierdo, A.; Tejedor, B.; Mañanes, R. Weak Wave–Tide Interaction Formulation and Its Application to Cádiz Bay. *Cont. Shelf Res.* **2001**, *21*, 697–725. [CrossRef]
31. Meinshausen, M.; Smith, S.J.; Calvin, K.; Daniel, J.S.; Kainuma, M.L.T.; Lamarque, J.-F.; Matsumoto, K.; Montzka, S.A.; Raper, S.C.B.; Riahi, K.; et al. The RCP Greenhouse Gas Concentrations and Their Extensions from 1765 to 2300. *Clim. Change* **2011**, *109*, 213–241. [CrossRef]
32. Korres, G.; Ravdas, M.; Zacharioudaki, A. Mediterranean Sea Waves Hindcast (CMEMS MED-Waves) 2019. [Data Set]. [CrossRef]
33. Tolman, H.L. User Manual and System Documentation of WAVEWATCH III R Version 4.18. Available online: https://polar.ncep.noaa.gov/waves/wavewatch/manual.v4.18.pdf (accessed on 29 December 2024).
34. Perez, J.; Menendez, M.; Mendez, F.J.; Losada, I.J. Evaluating the Performance of CMIP3 and CMIP5 Global Climate Models over the North-East Atlantic Region. *Clim. Dyn.* **2014**, *43*, 2663–2680. [CrossRef]
35. De Winter, R.C.; Sterl, A.; Ruessink, B.G. Wind Extremes in the North Sea Basin under Climate Change: An Ensemble Study of 12 CMIP5 GCMs. *JGR Atmos.* **2013**, *118*, 1601–1612. [CrossRef]
36. Griffies, S.M.; Danabasoglu, G.; Durack, P.J.; Adcroft, A.J.; Balaji, V.; Böning, C.W.; Chassignet, E.P.; Curchitser, E.; Deshayes, J.; Drange, H.; et al. OMIP Contribution to CMIP6: Experimental and Diagnostic Protocol for the Physical Component of the Ocean Model Intercomparison Project. *Geosci. Model Dev.* **2016**, *9*, 3231–3296. [CrossRef]
37. Goward Brown, A.J.; Neill, S.P.; Lewis, M.J. The Influence of Wind Gustiness on Estimating the Wave Power Resource. *Int. J. Mar. Energy* **2013**, *3–4*, e1–e10. [CrossRef]
38. Lobeto, H.; Menendez, M.; Losada, I.J. Future Behavior of Wind Wave Extremes Due to Climate Change. *Sci. Rep.* **2021**, *11*, 7869. [CrossRef] [PubMed]
39. Fanti, V.; Ferreira, Ó.; Kümmerer, V.; Loureiro, C. Improved Estimates of Extreme Wave Conditions in Coastal Areas from Calibrated Global Reanalyses. *Commun. Earth Environ.* **2023**, *4*, 151. [CrossRef]
40. Camus, P.; Mendez, F.J.; Medina, R. A Hybrid Efficient Method to Downscale Wave Climate to Coastal Areas. *Coast. Eng.* **2011**, *58*, 851–862. [CrossRef]
41. Booij, N.; Ris, R.C.; Holthuijsen, L.H. A Third-Generation Wave Model for Coastal Regions: 1. Model Description and Validation. *J. Geophys. Res.* **1999**, *104*, 7649–7666. [CrossRef]
42. Battjes, J.A.; Janssen, J.P. Energy Loss and Set-up Due to Breaking of Random Waves. In Proceedings of the Sixteenth Conference on Coastal Engineering, Hamburg, Germany, 27 August–3 September 1978; pp. 569–587. [CrossRef]
43. Hanna, S.R.; Heinold, D.W. *Development and Application of a Simple Method for Evaluating Air Quality*; Technical Report; American Petroleum Institute, Health and Environmental Affairs Dept: Washington, DC, USA, 1985.
44. Mentaschi, L.; Besio, G.; Cassola, F.; Mazzino, A. Problems in RMSE-Based Wave Model Validations. *Ocean Model.* **2013**, *72*, 53–58. [CrossRef]
45. Mentaschi, L.; Besio, G.; Cassola, F.; Mazzino, A. Performance Evaluation of Wavewatch III in the Mediterranean Sea. *Ocean Model.* **2015**, *90*, 82–94. [CrossRef]
46. Spanish Ministry of Agriculture, Food and Environment. Data from: Plan de Ecocartografías del litoral Español. 2012. Available online: https://www.miteco.gob.es/es/costas/temas/proteccion-costa/ecocartografias/ecocartografia-cadiz.html (accessed on 29 December 2024).
47. Garrity, N.J.; Battalio, R.; Hawkes, P.J.; Roupe, D. Evaluation of Event and Response Approaches to Estimate the 100-Year Coastal Flood for Pacific Coast Sheltered Waters. In *Coastal Engineering 2006*; World Scientific Publishing Company: San Diego, CA, USA, 2007; pp. 1651–1663. [CrossRef]
48. Viavattene, C.; Jiménez, J.A.; Ferreira, O.; Priest, S.; Owen, D.; McCall, R. Selecting Coastal Hotspots to Storm Impacts at the Regional Scale: A Coastal Risk Assessment Framework. *Coast. Eng.* **2018**, *134*, 33–47. [CrossRef]
49. Ferreira, O.; Viavattene, C.; Jiménez, J.A.; Bolle, A.; Das Neves, L.; Plomaritis, T.A.; McCall, R.; Van Dongeren, A.R. Storm-Induced Risk Assessment: Evaluation of Two Tools at the Regional and Hotspot Scale. *Coast. Eng.* **2018**, *134*, 241–253. [CrossRef]

50. Mentaschi, L.; Vousdoukas, M.; Voukouvalas, E.; Sartini, L.; Feyen, L.; Besio, G.; Alfieri, L. The Transformed-Stationary Approach: A Generic and Simplified Methodology for Non-Stationary Extreme Value Analysis. *Hydrol. Earth Syst. Sci.* **2016**, *20*, 3527–3547. [CrossRef]
51. Gornitz, V. Vulnerability of the East Coast, U.S.A. to Future Sea Level Rise. *J. Coast. Res.* **1990**, *9*, 201–237.
52. Liang, B.; Shao, Z.; Wu, G.; Shao, M.; Sun, J. New Equations of Wave Energy Assessment Accounting for the Water Depth. *Appl. Energy* **2017**, *188*, 130–139. [CrossRef]
53. Alfieri, L.; Burek, P.; Feyen, L.; Forzieri, G. Global Warming Increases the Frequency of River Floods in Europe. *Hydrol. Earth Syst. Sci.* **2015**, *19*, 2247–2260. [CrossRef]
54. Knutti, R.; Sedláček, J. Robustness and Uncertainties in the New CMIP5 Climate Model Projections. *Nat. Clim. Change* **2013**, *3*, 369–373. [CrossRef]
55. Vousdoukas, M.I.; Voukouvalas, E.; Annunziato, A.; Giardino, A.; Feyen, L. Projections of Extreme Storm Surge Levels along Europe. *Clim. Dyn.* **2016**, *47*, 3171–3190. [CrossRef]
56. Del Río, L.; Plomaritis, T.A.; Benavente, J.; Valladares, M.; Ribera, P. Establishing Storm Thresholds for the Spanish Gulf of Cádiz Coast. *Geomorphology* **2012**, *143–144*, 13–23. [CrossRef]
57. Ribeiro, A.S.; deCastro, M.; Costoya, X.; Rusu, L.; Dias, J.M.; Gomez-Gesteira, M. A Delphi Method to Classify Wave Energy Resource for the 21st Century: Application to the NW Iberian Peninsula. *Energy* **2021**, *235*, 121396. [CrossRef]
58. Wang, X.L.; Feng, Y.; Swail, V.R. Changes in Global Ocean Wave Heights as Projected Using Multimodel CMIP5 Simulations. *Geophys. Res. Lett.* **2014**, *41*, 1026–1034. [CrossRef]
59. Lemos, G.; Semedo, A.; Dobrynin, M.; Behrens, A.; Staneva, J.; Bidlot, J.-R.; Miranda, P.M.A. Mid-Twenty-First Century Global Wave Climate Projections: Results from a Dynamic CMIP5 Based Ensemble. *Glob. Planet. Change* **2019**, *172*, 69–87. [CrossRef]
60. Raposeiro, P.D.; Fortes, C.J.; Reis, M.T.; Ferreira, J.C. Development of A Methodology to Evaluate the Flood Risk at the Coastal Zone. Available online: https://repositorio.lnec.pt/handle/123456789/1002230 (accessed on 29 December 2024).
61. Sevieri, G.; Galasso, C.; D'Ayala, D.; De Jesus, R.; Oreta, A.; Grio, M.E.D.A.; Ibabao, R. A Multi-Hazard Risk Prioritisation Framework for Cultural Heritage Assets. *Nat. Hazards Earth Syst. Sci.* **2020**, *20*, 1391–1414. [CrossRef]
62. Canesi, L.; Sardella, A.; Vogler, R.; Kaiser, A.; Vaccaro, C.; Bonazza, A. Hazard Analysis and Vulnerability Assessment of Cultural Landscapes Exposed to Climate Change-Related Extreme Events: A Case Study of Wachau (Austria). *Heritage* **2024**, *7*, 1917–1934. [CrossRef]
63. Bonazza, A.; Sardella, A. Climate Change and Cultural Heritage: Methods and Approaches for Damage and Risk Assessment Addressed to a Practical Application. *Heritage* **2023**, *6*, 3578–3589. [CrossRef]
64. Pica, A.; Lämmle, L.; Burnelli, M.; Del Monte, M.; Donadio, C.; Faccini, F.; Lazzari, M.; Mandarino, A.; Melelli, L.; Perez Filho, A.; et al. Urban Geomorphology Methods and Applications as a Guideline for Understanding the City Environment. *Land* **2024**, *13*, 907. [CrossRef]